J|A|C|S
ARTICLES
Published on Web 07/28/2006

Physical Controls on Directed Virus Assembly at Nanoscale Chemical Templates

Chin Li Cheung,[‡,#] Sung-Wook Chung,*[,‡] Anju Chatterji,[§] Tianwei Lin,[§] John E. Johnson,[§] Saphon Hok,[‡] Julie Perkins,[‡] and James J. De Yoreo*[,‡]

Contribution from the Chemistry and Materials Science Directorate, Lawrence Livermore National Laboratory, 7000 East Avenue, Livermore, California 94551, and Department of Molecular Biology, The Scripps Research Institute, 10550 North Torrey Pines Road, La Jolla, California 92037

Received March 20, 2006; E-mail: chung20@llnl.gov; deyoreo1@llnl.gov

Abstract: Viruses are attractive building blocks for nanoscale heterostructures, but little is understood about the physical principles governing their directed assembly. In situ force microscopy was used to investigate organization of Cowpea Mosaic Virus engineered to bind specifically and reversibly at nanoscale chemical templates with sub-30 nm features. Morphological evolution and assembly kinetics were measured as virus flux and inter-viral potential were varied. The resulting morphologies were similar to those of atomic-scale epitaxial systems, but the underlying thermodynamics was analogous to that of colloidal systems in confined geometries. The 1D templates biased the location of initial cluster formation, introduced asymmetric sticking probabilities, and drove 1D and 2D condensation at sub-critical volume fractions. The growth kinetics followed a $t^{1/2}$ law controlled by the slow diffusion of viruses. The ability of poly(ethylene glycol) (PEG) to induce the lateral expansion of virus clusters away from the 1D templates suggests a significant role for weak interactions.

Introduction

Organizing nanostructures and functional molecules into deterministic patterns at surfaces is a fundamental challenge in nanotechnology.[1] Self-assembly methods[1,2] are generally limited to creation of uniform 2D films.[3,4] Printing methods,[5,6] which have the potential for organizing nanostructures through creation of chemical templates, can rarely achieve patterning below 50 nm, and then controlling orientations of individual nanostructures is difficult. One approach to achieving higher density of functionality and shorter range order is to use macromolecular complexes—such as virions—as programmable building blocks, either for synthesis of nanoparticles and nanowires or for precise placement of molecular moieties exhibiting optical and electronic functions.[3,7,8] Because these building blocks are typically tens of nanometers in size, they offer the possibility of organization using existing chemical patterning methods that operate at the length scale of 50−100 nm. Moreover, as their surface chemistry can be manipulated in a site-selective manner,[3,7,9,10] they naturally lend themselves to directed assembly of heterogeneous structures with controlled placement and orientation.

Understanding the physical principles governing directed macromolecular assembly is problematic using current theories based on small molecule epitaxial systems because the assembly in those systems is driven by strong ionic and covalent interactions and steric factors are of minimal importance.[11] Here we report results using in situ force microscopy to investigate the dynamics of virus organization at nanoscale chemical templates fabricated using scanned probe nanolithography (SPN).[12−14] By varying virus flux and inter-viral potential and measuring the time dependence of pattern morphology, we show that the physics of directed macromolecular assembly can be understood by combining principles governing small molecule epitaxy with those that drive colloidal condensation in confined systems.

[‡] Lawrence Livermore National Laboratory.
[§] The Scripps Research Institute.
[#] Present address: Department of Chemistry, University of Nebraska−Lincoln, Lincoln, NE 68588.

(1) Whitesides, G. M.; Mathias, J. P.; Seto, C. T. *Science* **1991**, *254*, 1312−1319.
(2) Whitesides, G. M.; Boncheva, M. *Proc. Natl. Acad. Sci. U.S.A.* **2002**, *99*, 4769−4774.
(3) Lee, S.; Mao, C.; Flynn, C.; Belcher, A. *Science* **2002**, *296*, 892−895.
(4) Murray, C. B.; Kagan, C. R.; Bawendi, M. G. *Annu. Rev. Mater. Sci.* **2000**, *30*, 545−610.
(5) Quist, A. P.; Pavlovic, E.; Oscarsson, S. *Anal. Bioanal. Chem.* **2005**, *381*, 591−600.
(6) Xia, Y. N.; Whitesides, G. M. *Annu. Rev. Mater. Sci.* **1998**, *28*, 153−184.
(7) Wang, Q.; Lin, T. W.; Tang, L.; Johnson, J. E.; Finn, M. G. *Angew. Chem., Int. Ed.* **2002**, *41*, 459−462.
(8) Mao, C.; Flynn, C.; Hayhurst, A.; Sweeney, R.; Qi, J.; Georgiou, G.; Iverson, B.; Belcher, A. *Proc. Natl. Acad. Sci. U.S.A.* **2003**, *100*, 6946−6951.
(9) Schlick, T. L.; Ding, Z. B.; Kovacs, E. W.; Francis, M. B. *J. Am. Chem. Soc.* **2005**, *127*, 3718−3723.
(10) Joshi, N. S.; Whitaker, L. R.; Francis, M. B. *J. Am. Chem. Soc.* **2004**, *126*, 15942−15943.
(11) Bartelt, M. C.; Hannon, J. B.; Schmid, A. K.; Stoldt, C. R.; Evans, J. W. *Colloid Surf. A: Physicochem. Eng. Asp.* **2000**, *165*, 373−403.
(12) Ginger, D. S.; Zhang, H.; Mirkin, C. A. *Angew. Chem., Int. Ed.* **2004**, *43*, 30−45.
(13) Liu, G. Y.; Xu, S.; Qian, Y. L. *Acc. Chem. Res.* **2000**, *33*, 457−466.
(14) Wouters, D.; Schubert, U. S. *Angew. Chem., Int. Ed.* **2004**, *43*, 2480−2495.

Experimental Section

Synthesis of the Functional Thiols for Nanoscale Chemical Templates. The synthesis of chemically modified alkanethiol linkers was accomplished using preparations similar to that previously reported.[15] Details regarding the synthetic procedures are described in Supporting Information (SI).

Fabrication of Nanoscale Chemical Templates and In Situ Scanning Force Microscopy (SFM). Flat gold substrates were prepared using a template-stripping method.[16] These substrates were then coated with poly(ethylene glycol) (PEG)-terminated alkanethiols that formed a self-assembled monolayer (SAM). To create the templates, a sharp silicon probe (Force modulation (FM) etched silicon probe, Nanosensor Gmb, Germany, average tip diameter is ca. 10 nm) in an atomic force microscope (CP Research AFM, Veeco Metrology, Inc., Fremont, CA) driven by customized lithographic software was used to apply high load force to "shave" linear trench patterns in the PEG-terminated alkanethiol SAM. The resulting trenches were filled with nickel(II)-chelated nitrilotriacetic acid (NTA)-terminated alkanethiols by immersing the sample in a 2 mM ethanol solution of the NTA thiol overnight and then in a 10 mM solution of aqueous nickel sulfate ($NiSO_4$) for 1 h. The sample was then rinsed with 18.5 MΩ water and dried with a stream of N_2 gas. It was then glued to a glass cover-slip on a sample holder and inserted into an atomic force microscope (AFM) liquid cell within a multimode AFM (Nanoscope IIIA, Digital Instruments and Veeco Metrology, Inc., Santa Barbara, CA). The AFM probe consisted of a sharp silicon tip on a silicon nitride cantilever (BIO97, spring constant = ca. 0.05 N/m, average tip diameter ~ 15 nm, NanoDevices, Veeco Metrology, Inc., Santa Barbara, CA). The AFM probe was prefunctionalized with 2-[methoxy(polyethylenoxy)propyl] trimethoxysilane (1 mM in 200 proof ethanol for 30 min) to minimize nonspecific adsorption of protein on its surface.[17]

Genetically engineered Cowpea Mosaic Virus (CPMV) was decorated with six contiguous histidine residues (His-CPMV) at geometrically equivalent sites on surface-exposed loops of the capsid by modifying the viral RNA.[18] High-resolution AFM images of typical His-CPMV particles are shown in Figure S2 (SI). Solution mixtures of freshly prepared His-CPMV and poly(ethylene glycol) 6k (PEG 6k, Aldrich-Sigma, St. Louis, MO) of various concentrations in 0.1 M HEPES buffer (pH = 7.25) were injected into the liquid cell assembly.

The evolution of the virus assembly on the chemical templates was imaged by tapping-mode at 0.5−2 Hz scan speed as a function of time. Note that the imaging condition of in situ AFM is slightly different from that of typical tapping-mode operation in aqueous liquid. Once the tip approached and engaged the surface of the chemical template in normal tapping-mode, the engage set point was carefully optimized to barely sense interactions between tip and substrate. This minimized the average forces exerted on the substrate during in situ AFM imaging and was required to minimize tip-induced perturbation during imaging. However, the images in Figure 1e still show a few partial His-CPMV particles (i.e., a half-moon shape or even smaller). While these may represent true detachment events, they may also be due to tip-induced detachment events during scanning. The cantilever of the AFM probe assembly was vibrated at f = ca. 30−35 kHz with a free cantilever oscillation RMS amplitude (A_0) of ca. 1.5 V. The amplitude set point was adjusted to maintain weak interactions for minimal perturbation, resulting in damping of the free amplitude by only 5−10%. The images were taken in the topographic imaging mode. Relatively high integral (1−3) and proportional (5−7) gains were required in the aqueous medium for stable imaging conditions. Time evolution in situ AFM images were analyzed to determine the average half-width of virus clusters by using image processing and analysis software (Scion Image, Scion Corporation, Frederick, MD).

Results and Discussion

Our chosen model system is Cowpea Mosaic Virus (CPMV) genetically engineered to present histidine (His) tags around the capsid apexes (Figure 1).[7,18,19,20] An AFM image of a CPMV film showing the pseudo-3-fold capsid geometry and its relation to CPMV molecular structure is given in Figure 1d. Atomically flat gold substrates were coated with self-assembled monolayers (SAMs) of poly(ethylene glycol) (PEG)-terminated alkanethiols to resist nonspecific virus attachment.[21,22] These were then patterned with nickel(II)-chelating nitrilotriacetic acid (Ni−NTA)-terminated alkanethiols (Figure 1a) using two-step nanografting[13,15] (Figure 1b) to produce linear templates (Figure 1c). The Ni−NTA features, which had minimum dimensions ranging from 10 to 100 nm and were separated by 50−1000 nm (Figure 1b), provided the chemoselective attachment sites for the His tags on the virions through a metal coordination complex (Figure 1a).[20]

We chose the Ni−NTA linker because it is a well-known immunolabeling compound for poly-His-tagged biomolecules.[23−27] Its small size compared to that of more commonly used antigen−antibody or a streptavidin−biotin pairs makes it ideal for efficiently localizing binding sites at molecular resolution with little steric hindrance.[28] Moreover, the binding constants of Ni−NTA[29] to His tags are high enough to give specificity ($K_D \sim 10^{-7}-10^{-9}$ M at pH approximately 7.0−8.0), but small compared to typical strong antigen−antibody interactions, such as avidin−biotin ($K_D \sim 10^{-15}-10^{-17}$ M), allowing for reversibility. Furthermore, because the strength of binding between Ni−NTA and His tags can be systematically varied through changes in pH[30] or addition of imidazole,[31] attachment/detachment processes are also tunable. (This is in contrast to previous ex situ studies of cysteine-modified CPMV (Cys-CPMV) attachment to maleimide-functionalized alkanethiols,[15,32] where bonding was covalent and nonreversible and inter-virion disulfide bonds could form, allowing for little control over assembly.)

In situ force microscopy was used to investigate the degree of ordering, packing geometry, assembly kinetics, and cluster-size distribution both on the Ni−NTA and the surrounding PEG-terminated regions. We emphasize that because this investigation

(15) Cheung, C. L.; Camarero, J. A.; Woods, B. W.; Lin, T. W.; Johnson, J. E.; De Yoreo, J. J. *J. Am. Chem. Soc.* **2003**, *125*, 6848−6849.
(16) Wagner, P.; Hegner, M.; Guntherodt, H. J.; Semenza, G. *Langmuir* **1995**, *11*, 3867−3875.
(17) Yam, C. M.; Xiao, Z. D.; Gu, J. H.; Boutet, S.; Cai, C. Z. *J. Am. Chem. Soc.* **2003**, *125*, 7498−7499.
(18) Chatterji, A.; Ochoa, W. F.; Ueno, T.; Lin, T. W.; Johnson, J. E. *Nano Lett.* **2005**, *5*, 597−602.
(19) Douglas, T.; Young, M. *Adv. Mater.* **1999**, *11*, 679−681.
(20) Medintz, I. L.; Sapsford, K. E.; Konnert, J. H.; Chatterji, A.; Lin, T. W.; Johnson, J. E.; Mattoussi, H. *Langmuir* **2005**, *21*, 5501−5510.
(21) Lopez, G. P.; Biebuyck, H. A.; Harter, R.; Kumar, A.; Whitesides, G. M. *J. Am. Chem. Soc.* **1993**, *115*, 10774−10781.
(22) Palegrosdemange, C.; Simon, E. S.; Prime, K. L.; Whitesides, G. M. *J. Am. Chem. Soc.* **1991**, *113*, 12−20.
(23) Hochuli, E.; Dobeli, H.; Schacher, A. *J. Chromatogr.* **1987**, *411*, 177−184.
(24) Hochuli, E.; Bannwarth, W.; Dobeli, H.; Gentz, R.; Stuber, D. *BioTechnol.* **1988**, *6*, 1321−1325.
(25) Hochuli, E.; Piesecki, S. *Methods: Companion Methods Enzymol.* **1992**, *4*, 41−56.
(26) Hoffmann, A.; Roeder, R. G. *Nucleic Acids Res.* **1991**, *19*, 6337−6338.
(27) Linder, P.; Guth, B.; Wulfing, C.; Krebber, C.; Steipe, B.; Muller, F.; Pluckthun, A. *Methods: Companion Methods Enzymol.* **1992**, *4*, 41−56.
(28) Buchel, C.; Morris, E.; Orlova, E.; Barber, J. *J. Mol. Biol.* **2001**, *312*, 371−379.
(29) Hainfeld, J. F.; Liu, W. Q.; Halsey, C. M. R.; Freimuth, P.; Powell, R. D. *J. Struct. Biol.* **1999**, *127*, 185−198.
(30) Paborsky, L. R.; Dunn, K. E.; Gibbs, C. S.; Dougherty, J. P. *Anal. Biochem.* **1996**, *234*, 60−65.
(31) Janknecht, R.; Demartynoff, G.; Lou, J.; Hipskind, R. A.; Nordheim, A.; Stunnenberg, H. G. *Proc. Natl. Acad. Sci. U.S.A.* **1991**, *88*, 8972−8976.
(32) Smith, J. C.; Lee, K. B.; Wang, Q.; Finn, M. G.; Johnson, J. E.; Mrksich, M.; Mirkin, C. A. *Nano Lett.* **2003**, *3*, 883−886.

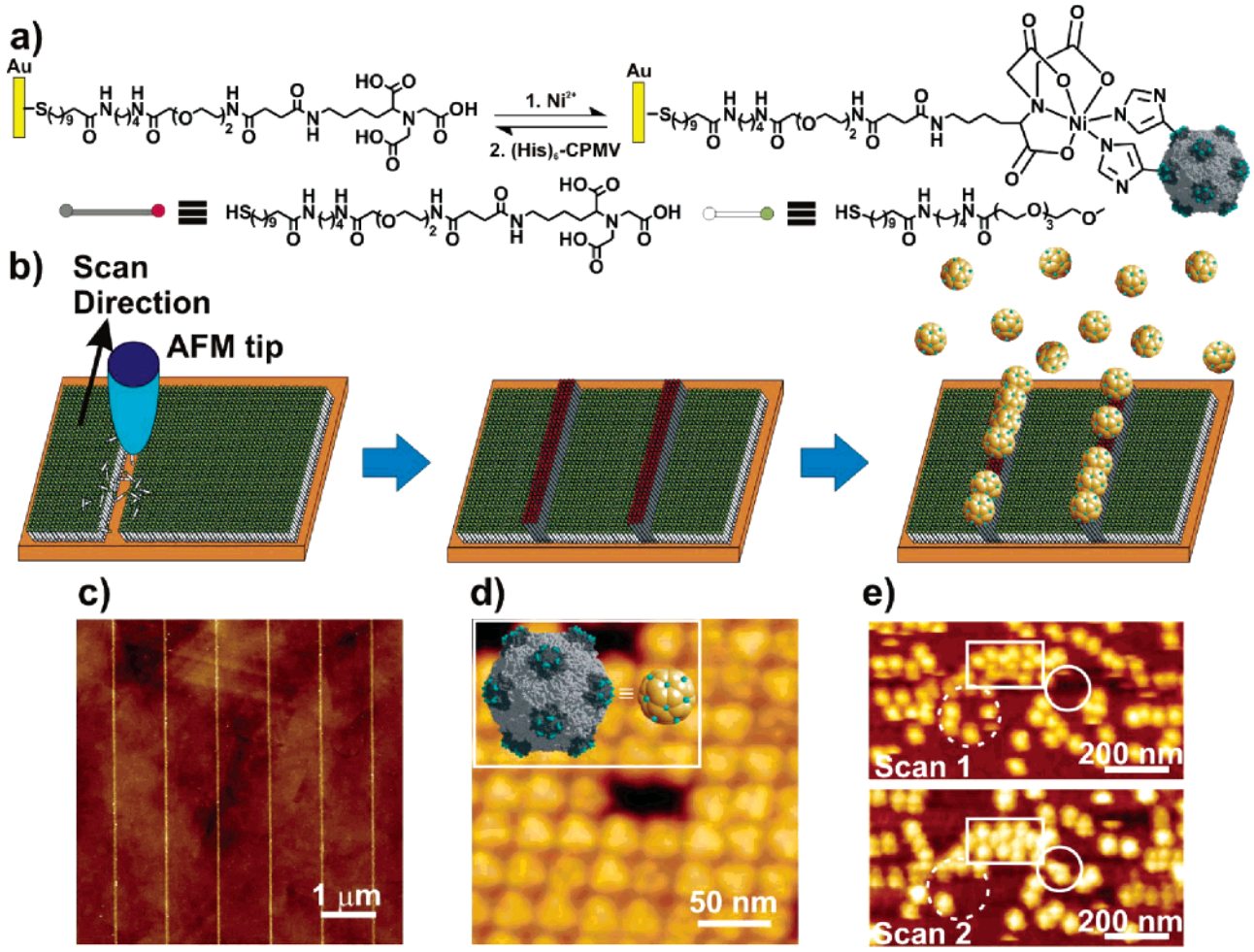

Figure 1. (a) Schematic of Ni(II) chelation reaction with NTA alkanethiol molecules bound to Au surfaces leading to reversible binding of His−CPMV to NTA-terminated regions and of molecular "inks" used for nanografting process. Short, PEG-terminated alkanethiol resists binding of CPMV (green headgroup); longer, NTA-terminated alkanethiol provides a reversible metal complex linkage to His tags engineered into CPMV (red headgroup). (b) Schematic of nanografting and virus deposition process. (c) AFM topographic (height) images of NTA-terminated line patterns (line width = ca. 25 nm) fabricated via nanografting on an atomically flat Au substrate. Note that the atomic steps of the {111} gold surface are visible beneath the SAM. Typical pitch distance between lines is from 100 nm to 2 μm patterned over 80 × 80 μm^2 area. (d) High-resolution AFM image of 2D wild-type CPMV film formed by evaporation on mica, illustrating the 3-fold symmetry of the virus. Inset shows the detailed structure of His−CPMV and its molecular model used in Figure 1b. Note that each capsid corner of His-CPMV contains six histidine tags (colored light blue). (e) Two consecutive AFM images of His−CPMV particle attachment and detachment on a Ni−NTA-terminated Au surface. Time interval between images is 10 min. Solid circle, dashed circle, and rectangular box emphasize attachment of new His−CPMV virions, detachment of isolated virions, and stable, ordered clusters, respectively. The half-moon-shaped particles that are evident in a number of locations show individual virions that are attaching or detaching during imaging.

of directed assembly at templates was done in situ, the observed kinetics and morphological evolution is not driven by capillary forces as is commonly the case for studies of colloidal films formed through evaporation. To illustrate the dynamics of His−CPMV binding to Ni−NTA, Figure 1e shows two consecutive in situ AFM images of simultaneous His−CPMV particle attachment and detachment events at a uniform Ni−NTA SAM on a Au surface. The dashed and solid circles highlight examples for virions either isolated from or adjacent to one or two others. In contrast, the solid rectangular box outlines a relatively stable, ordered cluster of virions showing no detachments. Although it is likely that, even with a minimal perturbation, imaging assists detachment to some degree, these results show that the binding of His−CPMV virions on Ni−NTA-terminated surfaces is reversible with both attachment and detachment events occurring simultaneously.[33]

Figure 2 shows the evolution of His−CPMV assembly on Ni−NTA line patterns as a function of flux and inter-viral interaction, for line width equal to virus diameter (~28 nm). Virus flux was controlled by varying its solution concentration (C_V), and the inter-viral interaction was altered through an addition of PEG polymer (average MW ~ 6000 Da) to solution. The 6k PEG is a weakly interacting, nonadsorbing polymer additive that promotes nucleation and growth of bulk virus crystals,[34] including CPMV,[35−37] by creating an osmotic force associated with polymer exclusion.[38−41]

(33) We note that the possibility of picking up and redepositing a virus is minimal because the imaging tips have been functionalized with PEG as described in the Supporting Information.
(34) Mcpherson, A. *Methods Enzymol.* **1985**, *114*, 112−120.
(35) Johnson, J. E.; Hollingshead, C. *J. Ultrastruct. Res.* **1981**, *74*, 223−231.
(36) White, J. M.; Johnson, J. E. *Virology* **1980**, *101*, 319−324.
(37) Lin, T. W.; Chen, Z. G.; Usha, R.; Stauffacher, C. V.; Dai, J. B.; Schmidt, T.; Johnson, J. E. *Virology* **1999**, *265*, 20−34.
(38) Annunziata, O.; Asherie, N.; Lomakin, A.; Pande, J.; Ogun, O.; Benedek, G. B. *Proc. Natl. Acad. Sci. U.S.A.* **2002**, *99*, 14165−14170.
(39) Kulkarni, A. M.; Chatterjee, A. P.; Schweizer, K. S.; Zukoski, C. F. *J. Chem. Phys.* **2000**, *113*, 9863−9873.

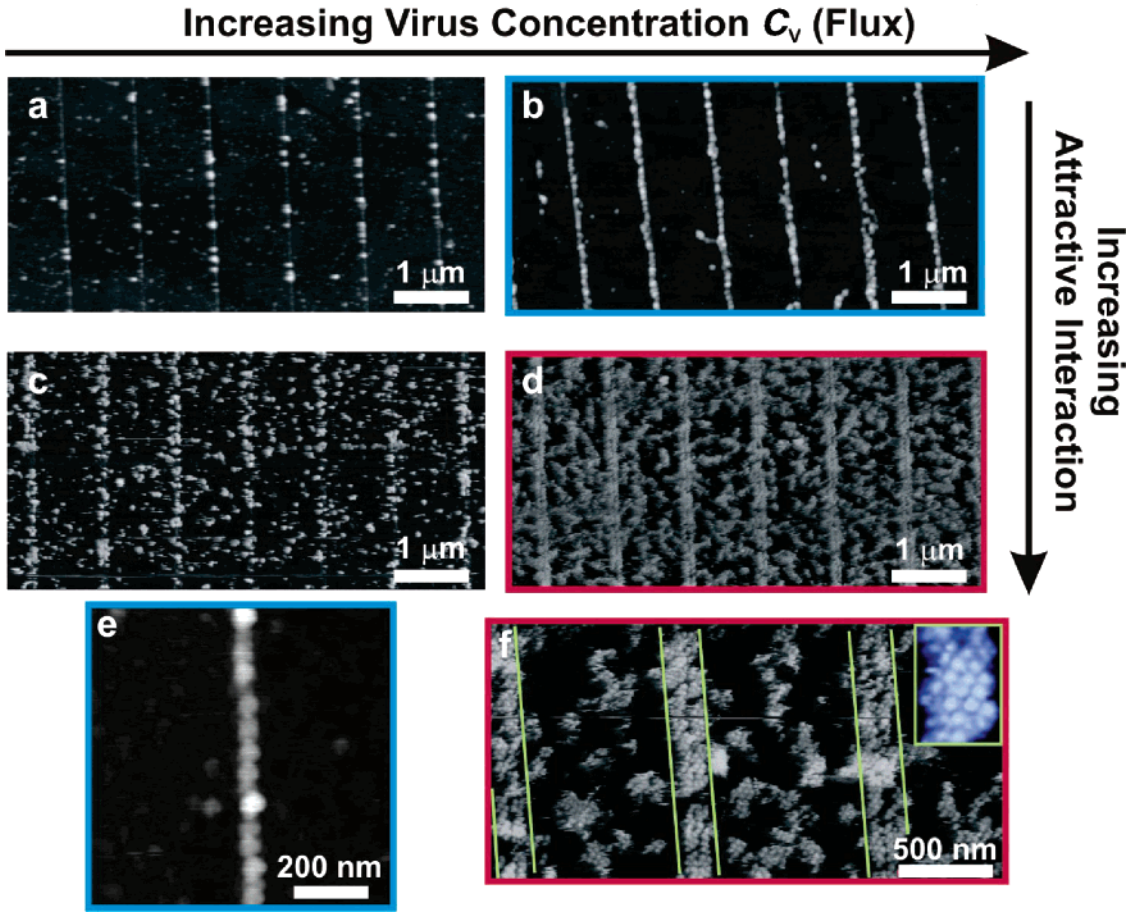

Figure 2. In situ AFM images showing evolution of coverage and order during His−CPMV adsorption as the virus flux (i.e., virus concentration (C_V)) and inter-viral interaction (i.e., PEG concentration) are increased. At low flux ($C_V \approx 0.2$ mg/mL) and 0% PEG (w/w) (a), His−CPMV attaches almost exclusively to Ni−NTA lines, but with poor coverage. At higher flux ($C_V \approx 2$ mg/mL) and weak interaction (0% PEG) (b), virions still attach to the Ni−NTA lines, but the lines are fully covered. As the inter-viral interaction is increased ($C_V \approx 0.5$ mg/mL, 1 wt % PEG for (c) and $C_V \approx 2$ mg/mL, 1 wt % PEG for (d)), virus assembly spreads outward from the lines to give stripes that are multiple virions in width and clusters lying between the lines. (e) Higher resolution AFM image of condition (b) showing the single line of His−CPMV particles. (f) High-resolution image of condition (d) showing a packing geometry similar to that seen for the ordered virus cluster in Figure 1e. Times at which images were collected are (a) 4, (b) 8, (c) 4, and (d) 6 h.

At low virus flux ($C_V = 0.1-0.2$ mg/mL) and relatively weak inter-viral interaction (i.e., no PEG addition), His−CPMV particles bind almost exclusively along the Ni−NTA lines but with coverage of ca. 20% or less (Figure 2a). As flux increases, virus density increases, and it approaches full coverage at 10 times higher flux ($C_V \cong 2.0$ mg/mL) (Figure 2b,e). As Figure 2e shows, to the extent that the symmetry of the virions is discernible, they appear to be oriented with the 3-fold axis perpendicular to the surface, similar to that seen in the 2D film formed by evaporation in Figure 1d.

As we turned on the attractive inter-viral interaction by increasing the concentration of PEG polymer, we observed several important changes at both low ($C_V \cong 0.5$ mg/mL) and high flux ($C_V \cong 2$ mg/mL) (Figure 2c,d). First, assembly begins on the lines but spreads laterally to give stripes of multiple virus rows. Second, disordered clusters form between lines where there is no Ni−NTA recognition site. Figure 2f shows three of the stripes, and the inset gives a higher resolution view, which reveals the same locally ordered packing observed in a small, stable cluster of Figure 1e. The stripes all have the same width and consist of six to seven full rows of virions. (Due to hexagonal packing, this gives a full width of only four virus diameters.) To emphasize the important role of these solvent-mediated inter-viral interactions in driving self-assembly, we note that when these samples are removed from the solution and rinsed, only the virions attached to the Ni−NTA lines remain. This is in stark contrast to the results obtained when direct inter-viral interactions are introduced through cysteine modifications.[15]

We also observed the evolution of His−CPMV assembly on linear templates as a function of time and flux (Figure 3a). Figure 3b gives the measured time dependence of the half-width of "on-line" stripes and the radius of "off-line" clusters. If we fit these data with a typical power law growth curve of the form At^{α}, a least-squares fit gives exponents α of 0.5 and 0.6 for the on-line and off-line domains, respectively. But given the scatter in the data, these two values are indistinguishable, and both curves are consistent with a power law of the form $At^{1/2}$, with $A = 0.13$ for on-line stripes and $A = 0.10$ for off-line clusters.

We can qualitatively understand the morphological and kinetic behavior by considering the principles developed to describe two contrasting systems: thin film epitaxy of atomic species and condensation of noninteracting colloids. During nucleation

(40) Budayova, M.; Bonnete, F.; Tardieu, A.; Vachette, P. *J. Cryst. Growth* **1999**, *196*, 210−219.
(41) Casselyn, M.; Perez, J.; Tardieu, A.; Vachette, P.; Witz, J.; Delacroix, H. *Acta Crystallogr. D* **2001**, *57*, 1799−1812.

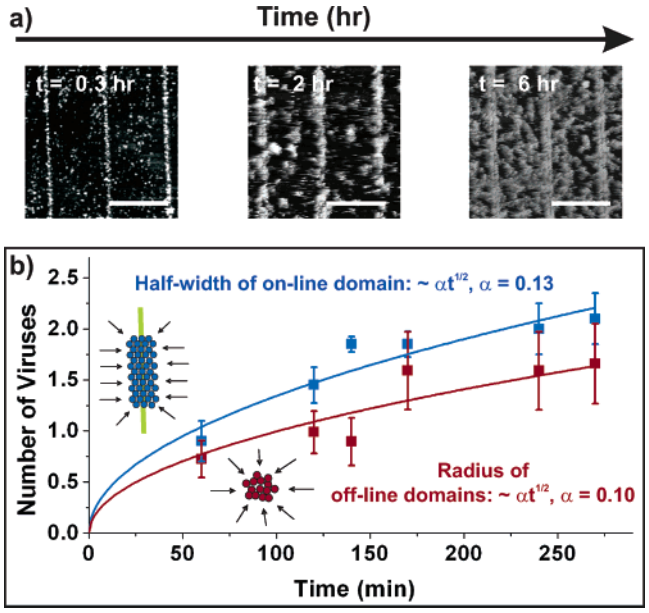

Figure 3. (a) Time series of in situ AFM images showing the evolution of a virus pattern for $C_V \approx 2$ mg/mL and PEG solution concentration of 1 wt %. (b) Analysis of time series in (a) showing the variation in half-width and radius of the on-line stripes (blue curve) and off-line clusters (red curve). Note that for the on-line stripes, due to the close-packing geometry, a half-width of two (full-width of four) actually corresponds to a stripe with six to seven full rows of virions, as indicated by the inset cartoon. The inset cartoons also show how the presence of the line alters the assembly morphology by creating a line of high sticking probability. In contrast, lower sticking probability leads to slower growth of off-line clusters. Solid lines are fits to the data of the form $At^{1/2}$, constrained to pass through (0,0). A = 0.13 for on-line domains and 0.1 for off-line clusters (r^2 = 0.92 and 0.86, respectively).

and growth of submonolayer atomic films, the number density and morphology of 2D islands is controlled by the competition between the applied flux of adatoms and the atomic mobility.[11] A higher ratio of flux to surface mobility gives a higher island number density. Increasing the ratio of flux to mobility at the atomic steps that form the edges of the islands results in increasingly dendritic island morphologies, eventually leading to the extreme of diffusion-limited aggregation (DLA).[42,43] At the other extreme, when mobility is high and flux is low, islands are compact, having smooth edges and shapes determined by the orientational dependence of step edge free energy.[44]

We can describe the island morphology in our virus system with the same principles (Figure 4). For a given surface and template chemistry (virus mobility), as concentration (flux) of virions increases, number density and cluster size increase (Figure 2c,d). As inter-viral interaction strength increases (through PEG addition), detachment rate and edge diffusivity decrease, thus cluster size increases and the shape becomes less compact (Figure 2b,d and Figure 4). For His−CPMV, island morphology is intermediate between compact and dendritic, progressing from the former to the latter as the flux or PEG concentration is increased (Figure 2a−d). This is similar to what is observed in atomic-scale epitaxial systems as diffusivity is decreased through reduction of substrate temperature.[42] For Cys−CPMV, formation of disulfide bonds between virions magnifies this phenomenon. Thus, island morphology was observed to be dendritic even without the addition of PEG[15] and is reminiscent of DLA with asymmetric sticking (Figure 4, upper right panel; see ref 15, Figure 2c for a large scale view). The role of the template is to bias the location of nucleation and, in the case of the 1D templates used here, create a high sticking probability and low detachment rate at the ends of the island, leading to linear shapes.

Despite similarities in morphological evolution, the thermodynamic driving force for condensation in these systems is completely different. In atomic epitaxial systems, nucleation and growth is driven by an excess surface concentration of adatoms over the equilibrium value, that is, the supersaturation. The vapor pressure is nearly zero, and every adatom deposited becomes a permanent member of the surface population, whether as part of an island or in the 2D reservoir of adatoms between the islands. As long as there is a flux to the surface, growth will continue, leading to multilayer growth of a bulk film because the supersaturation is always positive. Entropic factors play a minor role in driving condensation because growth is controlled by the strong covalent interactions between the atomic species.

In contrast, the thermodynamics of virus condensation is analogous to condensation of noninteracting colloids, which is completely driven by entropic factors.[45] Above a certain volume fraction, Φ_c, colloids take on a close-packed geometry through phase separation in order to maximize the free volume of water.[45] The introduction of various external factors, including alternating electric fields, polymer solutions, and surfaces, reduces the value of Φ_c.[46,47] When the distance between particles is comparable to or smaller than the polymer diameter, they experience an unbalanced osmotic pressure arising from the exclusion of polymer from the interparticle regions. To maximize the transitional entropy of the polymer, the inaccessible volume is minimized by driving the particles together, thereby introducing an attractive force that drives down Φ_c. The presence of a surface creates a near-surface region where the free volume of the solvent is decreased and induces condensation of a single monolayer at $\Phi < \Phi_c$. As Φ is increased toward Φ_c, the number of condensed layers increases until, at $\Phi = \Phi_c$, there is divergence toward a bulk condensate.

In analogy to the colloidal system, although virus condensation occurs at the templates, our solutions are never supersaturated (i.e., $\Phi < \Phi_c$). Not only do bulk condensates fail to grow, but we did not observe formation of second layer islands even though there is a continuous flux to the surface. Through the introduction of an osmotic force, addition of PEG to the solution leads to greater condensation, increasing the free volume of PEG near the surface. However, despite this analogy, the introduction of the 1D template makes the virus system studied here unique because it is no longer described simply by condensation at a uniform 2D surface in a 3D system. Nonetheless, the principles of assembly carry over if we view the linear template as a "1D surface" in a 2D system. At low volume fraction, virions do not condense in 2D, while the introduction of the 1D surface leads to formation of a "mono-line" of virions. The addition of

(42) Bales, G. S.; Chrzan, D. C. *Phys. Rev. Lett.* **1995**, *74*, 4879−4882.
(43) Roder, H.; Bromann, K.; Brune, H.; Kern, K. *Phys. Rev. Lett.* **1995**, *74*, 3217−3220.
(44) Theis, W.; Tromp, R. M. *Phys. Rev. Lett.* **1996**, *76*, 2770−2773.
(45) Cheng, Z. D.; Russell, W. B.; Chaikin, P. M. *Nature* **1999**, *401*, 893−895.
(46) Poon, W. C. K. *J. Phys.: Condens. Mater.* **2002**, *14*, R859−R880.
(47) van Blaaderen, A. *MRS Bull.* **2004**, *29*, 85−90.

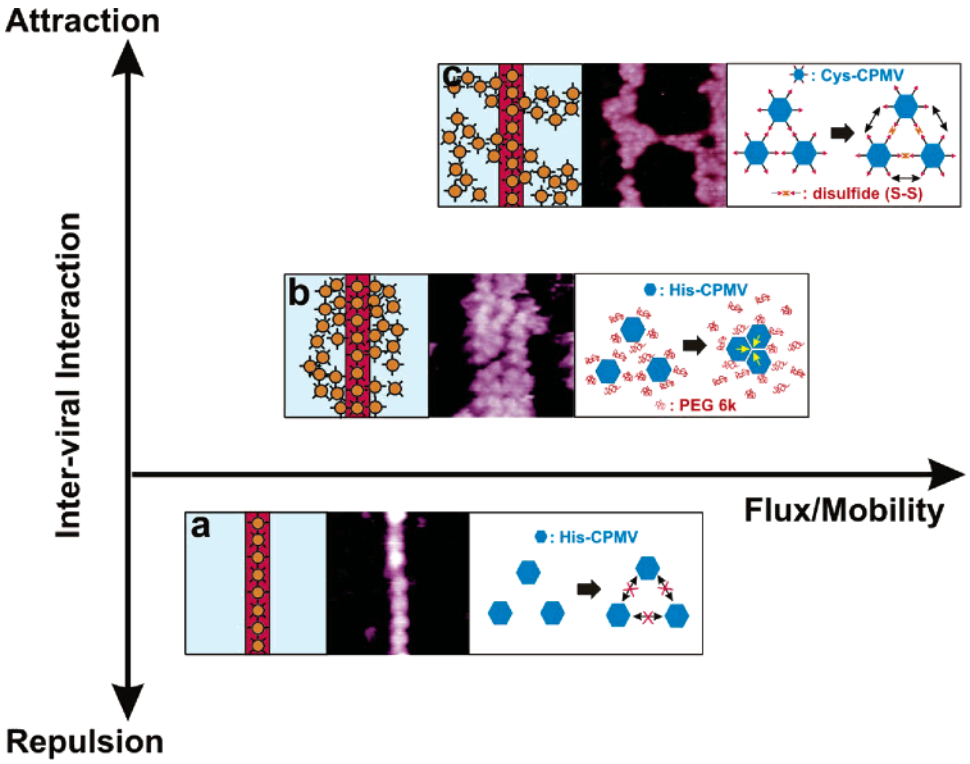

Figure 4. Structural diagram of virus assembly controlled by inter-viral interaction and virus flux/mobility. The variables of inter-viral interaction potential, virus flux, and surface mobility can be used to control the length scale and degree of virus ordering during assembly. When the interaction is weak or repulsive, 1D structures are formed as a result (Figure 4a). At high values of flux-to-mobility and/or strongly attractive interactions as it the case for Cys−CPMV,[15] dendritic patterns will arise due to the high attachment rates and slow rates of relaxation (Figure 4c from ref 15; larger length scale images are available there). At intermediate levels of flux/mobility and moderately attractive interactions, relaxation rates will be sufficient to lead to the growth of ordered stripes (Figure 4b), where the width of the stripes is determined by the thermodynamics of 2D film formation in the presence of 1D interfaces. The scan size of each AFM image is 500 nm × 500 nm.

PEG introduces an osmotic force that both causes the condensation of virus in 2D at a volume fraction that is too low to do so in the absence of the surface and leads to the expansion of the 1D film to two mono-lines, then three, etc. For the conditions shown in Figure 2, the limiting value appears to be about seven mono-lines.

The $t^{1/2}$ law that describes the growth kinetics can be understood by considering the controls of diffusion to the surface and attachment at island edges, the first being a characteristic of colloidal systems and the second a common phenomenon in small molecule epitaxy. First, the surface concentration must be obtained by solving the diffusion equation because there is no other mechanism of transport to the surface in an unmixed AFM liquid cell. The system consists of a cylindrical solution volume bounded on the top and cylindrical sides by nonreacting surfaces and on the bottom face by a surface which removes viruses from solution at a rate proportional to the excess concentration. At time $t = 0$, the solution has a uniform virus concentration. The characteristic diffusion length is $\sim(Dt)^{1/2}$, where D is the diffusivity of CPMV in solution. On the time scale of our measurements (1−5 h), and for virus diffusivity of $<10^{-7}$ cm^2 s^{-1},[48] the diffusion length is ∼100 μm. Because this is much less than the distance to the cell walls, we can approximate the system as a semi-infinite volume bound by the bottom surface. Because the characteristic diffusion length is also much greater than the spacing between islands, we can approximate the surface concentration as a constant across the surface. The boundary condition at the bottom surface is then equivalent to a radiation condition and is given by[49]

$$D\frac{\partial C}{\partial n} = -H(C - C_e) \qquad (1)$$

where C is the actual virus concentration, n is the unit vector normal to the surface, and H is a rate coefficient. In this case, C_e is the concentration of the solution at which deposition onto the substrate goes to zero. This is not the solubility of CPMV, which in these experiments is greater than the actual concentration. The solution to the diffusion equation for this geometry and boundary condition has an exact solution, which at the surface is given by[49]

$$(C - C_e)|_{x=0} = (C - C_e)|_{t=0} e^{h^2 Dt} erfc(h\sqrt{Dt}) \qquad (2)$$

where $h = H/D$. At long times, this becomes[49]

$$(C - C_e)|_{x=0} = (C - C_e)|_{t=0} (h\sqrt{\pi Dt})^{-1} \qquad (3)$$

where the relative error in $(C - C_e)$ at $x = 0$ is less than $D/(2H^2t)$.[50]

The value of H can be estimated from the measured flux to the surface. The total amount of virus deposited at long times over the range of concentrations used here is of the order 0.1−0.3 monolayers. This dissolved in a cell volume of 80 μL gives

(48) The diffusivity of CPMV has not been measured, but the diffusivity of large proteins is 10^{-6}−10^{-7} cm^2 s^{-1}. See for example: Petsev, D. N.; Vekilov, P. G. *Phys. Rev. Lett.* **2000**, *84*, 1339−1342. Scaling the diffusivity by the hydrodynamic radius leads to a value of $\leq 10^{-7}$ cm^2 s^{-1}.

an initial value of $C - C_e = 3 \times 10^{11}$ particles·cm^{-3}. The initial rate of deposition onto the surface, that is, the flux, is about 0.1 monolayers in 10^3 s, or 1.5×10^7 particles·cm^{-2} s^{-1}. Taking $D = 10^{-7}$ cm^2 s^{-1} gives an error of <2% for $t > 1000$ s, so the approximation leading from eq 2 to eq 3 is justified. This derivation shows that, although transport of viruses to the surface is by diffusion, the adsorption kinetics control the boundary condition at $x = 0$ and affect the magnitude of the surface concentration through the parameter H.

Taking the net attachment rate to be linear in excess concentration, as is typically observed for solution deposition and expected for rough step edges,[51,52] the speed of an island edge dr/dt is

$$\frac{dr}{dt} = \beta(C - C_e)|_{x=0} \tag{4}$$

where β is referred to as the kinetic coefficient and reflects the barriers to attachment and detachment, as well as geometric factors.[51,52] Combining eqs 3 and 4 and integrating gives

$$r(t) = At^{0.5} \text{ with } A = \frac{2\beta(C - C_e)|_{t=0}}{h(\pi D)^{0.5}} \tag{5}$$

explicitly showing that the square root law arises from the diffusion control over virus flux to the surface, combined with the linear kinetics of attachment at the island edges. Differences between the on-line and off-line sticking probabilities and detachment frequencies result in differences in the value of the prefactor A.

Another important difference between the situation described here and that of small molecule epitaxial systems is that the dependence of C_e on size due to the excess free energy of the step as given by the Gibbs−Thomson relationship[53] does not apply here. This is because condensation is driven by the entropic factors and the enthalpic terms that give rise to that excess free energy are unimportant. This is reflected in the observations that clusters do not grow into three dimensions and, as island size increases, the growth rate slows rather than increases as expected from the Gibbs−Thomson law.

The physical picture of directed macromolecular assembly that emerges from this investigation combined with previous observations using Cys-modified CPMV[15] is summarized in Figure 4. The final pattern morphology and degree of order can be modulated by varying the intermolecular interaction and/or the ratio of flux to mobility. The intermolecular interaction can be tuned either through introduction of entropic forces or by engineering in mutual binding sites, and the mobility can be varied by changing the template chemistry. As a result, patterns can be achieved that range from single lines to compact domains to interconnected dendrites. Finally, the asymmetry in those patterns is determined through the choice of template geometry. The challenge for the future is to utilize platforms such as the one presented here to complete the quantitative foundation for this physical picture by applying analyses of assembly dynamics similar to those that have led to a rigorous understanding of small molecule epitaxy[11] and colloidal condensation.[45−47]

Acknowledgment. We acknowledge the contributions of Julio A. Camarero to the initial development of synthetic methods, and Cherry A. Murray to the development of the kinetic analysis. J.D.Y., S.W.C., and C.L.C. acknowledge U.S. Department of Energy (DOE), Office of Basic Energy Science (BES), Division of Chemical Sciences, Geosciences, and Biosciences for support of this research. T.L. and J.E.J. acknowledge the support of Office of Naval Research (ONR) (Grant Nos. N00014-03-1-0632 and N00014-00-1-0671). This work was performed under the auspices of the U.S. Department of Energy by the University of California, Lawrence Livermore National Laboratory under Contract No. W-7405-Eng-48.

Supporting Information Available: Detailed experimental procedures for the preparations of functional alkanethiol linkers, characterization data, and additional AFM images of virus particles. This material is available free of charge via the Internet at http://pubs.acs.org.

JA0616884

(49) Carslaw, H. S.; Jaeger, J. C. *Conduction of Heat in Solids*, 2nd ed.; Clarendon Press: Oxford, 1959; Vol. viii, p 510.
(50) Note that the concentration eventually decreases to the equilibrium bulk concentration. However, eq 3 predicts an infinite decay time when, in reality, the time is finite due to the finite dimensions of the liquid cell. That is, the assumed boundary conditions leading to eq 3 are no longer applicable once Dt is comparable to the AFM liquid cell dimensions.
(51) Chernov, A. A. *Modern Crystallography III: Crystal Growth*; Springer-Verlag: Berlin, 1984; Vol. 36, p 517.
(52) De Yoreo, J. J.; Vekilov, P. *Biomineralization*; Mineralogical Society of America: Washington, DC, 2003; Vol. 54, p 381.
(53) In typical epitaxial systems, the right-hand side of eq 4 is not independent of r for small island sizes. This is because one must take into account the size dependence of the C_e as given by the Gibbs−Thomson equation, $C_e = C_e^\infty \exp(a\gamma/k_B Tr)$, where C_e^∞ is equilibrium concentration for the bulk solid, a is the area per molecule in the film, γ is the excess free energy per molecule associated with adding molecules to the edge of the island over that of the infinite flat layer, and k_B is Boltzmann's constant. However, in small molecule systems, γ comes from the enthalpic term in the free energy associated with reduced coordination along the step edge relative to the interior of the island, which in turn comes from the strong intermolecular bonding in the condensed phase. Because colloidal condensation at a surface is driven by increasing the entropy of the solvent near the surface, this enthalpic effect is unimportant. Thus, once nucleated, clusters do not continue to grow into three dimensions and their growth rate does not increase with size as would be expected from the Gibbs−Thomson law.